Signal Processing 101 (2014) 19–34

Contents lists available at ScienceDirect

Signal Processing

journal homepage: www.elsevier.com/locate/sigpro

A spatially adaptive retinex variational model for the uneven intensity correction of remote sensing images

Xia Lan [a,b], Huanfeng Shen [c,*], Liangpei Zhang [d], Qiangqiang Yuan [e]

[a] School of Mathematics and Statistics, Wuhan University, Wuhan 430072, PR China
[b] The 10th Institute of China Electronics Technology Group Corporation, Chengdu 610036, PR China
[c] School of Resource and Environmental Science, Wuhan University, Wuhan 430079, PR China
[d] The State Key Laboratory of Information Engineering in Surveying, Mapping and Remote Sensing, Wuhan University, Wuhan 430079, PR China
[e] School of Geodesy and Geomatics, Wuhan University, Wuhan 430079, PR China

ARTICLE INFO

Article history:
Received 30 May 2013
Received in revised form
6 December 2013
Accepted 17 January 2014
Available online 30 January 2014

Keywords:
Uneven intensity correction
Variational method
Spatially adaptive
Remote sensing images

ABSTRACT

In this paper, a spatially adaptive retinex variational model for the uneven intensity correction of remote sensing images is proposed. In the model, the spatial information is used to constrain the TV regularization strength of the reflectance. In the edge pixels, a weak regularization strength is enforced to preserve detail, and in the homogeneous areas, a strong regularization strength is enforced to eliminate the uneven intensity. The relationship and the fidelity term between the illumination and reflectance are also considered. Moreover, the split Bregman optimization algorithm is employed to solve the proposed model. The experimental results with both simulated and real-life data demonstrate that the proposed method is effective, based on both the visual effect and quantitative assessment.

1. Introduction

It is well known that the remote sensing image acquisition process is complicated, which usually results in radiometric errors. The two main reasons for the errors are sensor malfunction and the external interference. Even if the imaging system is in working order, radiometric errors will still accompany the external interference. The external factors include: non-uniform illumination; atmospheric attenuation brought about by atmospheric scattering and absorption; and terrain attenuation brought about by terrain elevation, aspect, slope, and so on. Therefore, remote sensing images usually have an uneven intensity distribution, color cast, etc. In this paper, we are concerned with the uneven intensity distribution that is caused by the non-uniform illumination in aerial remote sensing images. Since remote sensing data is very important for image classification, change detection, and other applications [1–3], it is extremely important to carry out radiometric correction.

The traditional correction methods are either absolute or relative radiometric correction. Most forms of absolute radiometric correction are based on physical theory, which is extremely complex. This often requires huge amounts of information, including atmospheric and sensor properties for the acquisition date of the satellite scene, and so on. For the majority of the archived satellite images, this information is not available [4–6]. Thus, relative radiometric correction has been developed, which normalizes multiple satellite scenes to match a referenced one. To date, a few methods based on single-scene image enhancement have been applied to adjust uneven illumination, including the homomorphic filter (HF) and histogram equalization (HE). The HF can adjust the illumination, but it suffers from the problem of color distortion [7–9]. The HE can redistribute the intensity distribution [9–13]; however, the results may sometimes turn out to be even more

---

* Corresponding author. Tel.: +86 13163235536
E-mail addresses: lanxia2008@whu.edu.cn (X. Lan), shenhf@whu.edu.cn (H. Shen), zlp62@lmars.whu.edu.cn (L. Zhang), yqiang86@gmail.com (Q. Yuan).

0165-1684/$ - see front matter © 2014 Elsevier B.V. All rights reserved.
http://dx.doi.org/10.1016/j.sigpro.2014.01.017

uneven [9]. Furthermore, a unique solution does not exist for multiband histogram matching [14].

Color perception techniques based on the human visual system (HVS) have also been developed to correct the uneven intensity distribution [6]. When the illumination level is very low, the rods in the retina play a leading role. Thus, the HVS cannot identify the color very well [15–17]. However, the HVS has the ability to perceive the colors of a scene almost independently of the spectral electromagnetic composition of uniform illumination, i.e., color constancy [6]. The first contribution in this field was the retinex theory proposed by Land and McCann [18,19]. Subsequently, other path-based algorithms have been proposed based upon different path geometry [20–22]; however, these approaches can be time-consuming.

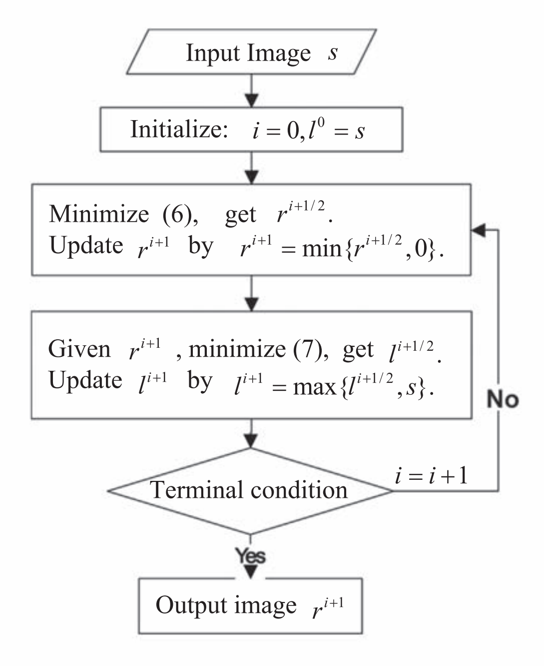

Fig. 1. The basic procedure for the alternating minimization. Terminal condition: $(||r^{i+1}-r^i||/||r^{i+1}||) \le \varepsilon_r$ and $||l^{i+1}-l^i||/||l^{i+1}|| \le \varepsilon_l$.

In the image processing field, PDE-based models and variational techniques have been very popular [23–26], and have also been developed for uneven intensity correction. According to retinex theory, researchers have decomposed the image intensity as a product of the illumination and reflectance intensity. With the assumption that the illumination varies smoothly, Poisson equation type retinex algorithms have been proposed [27–30]. Based on this assumption, a variational framework for the retinex was proposed by Kimmel et al. [31]. In this framework, the illumination intensity is first estimated by a variational model, and it is then removed to obtain the reflectance intensity. Recently, according to the reflectance piecewise constant assumption, Michael et al. [32] and Li et al. [6] proposed a total variation (TV) model and a perceptually inspired variational method for the retinex, respectively. In [32], the relationship and the fidelity term between the illumination and reflectance are considered. In [6], both the L2 norm prior and the TV prior are used; furthermore, the “gray world” (GW) assumption [33] is also considered. Although these methods did show improvements, there are still shortcomings with both models.

In this paper, a spatially adaptive retinex variational model is proposed. Here, the spatial information is used to constrain the TV regularization strength of the reflectance. In the edge pixels, a weak regularization strength is enforced to preserve detail, and in the homogeneous areas, a strong regularization strength is enforced to eliminate the uneven intensity. In addition, we take the essentials features of both [6,32], in that the GW assumption and the fidelity term between the illumination and reflectance are also considered in the proposed model. Moreover, the split Bregman optimization algorithm is employed to solve the proposed model.

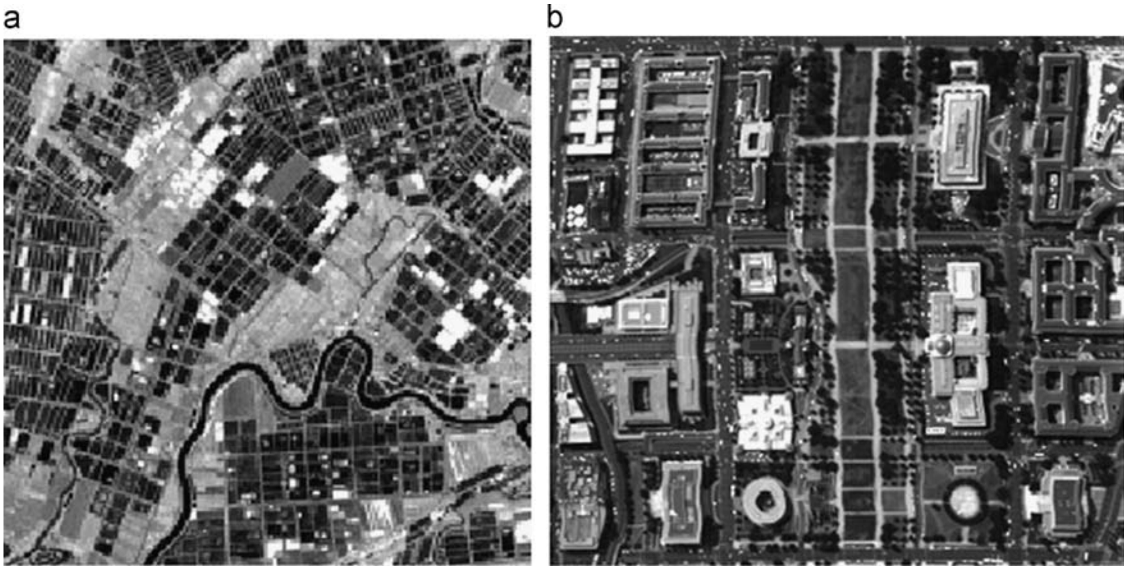

Fig. 2. The original standard images. (a) Wuhan in China. (b) Washington DC.

The remainder of this paper is organized as follows. In Section 2, we review retinex theory and the perceptually inspired retinex variational framework. The spatially adaptive retinex variational model is described in detail in Section 3. The experiments are presented in Section 4. Finally, conclusions are drawn in Section 5.

2. The retinex framework

2.1. Retinex theory

Recently, more attention has been paid to color perception techniques based on the HVS [6,34]. Here, we review the first contribution in this field: retinex theory. The basic model is as follows:

$$S = L \cdot R \tag{1}$$

where S is the observed image, L is the uneven or even illumination distribution, and R represents the object reflectance ($0 \le R \le 1$), which is related to the physical characteristics of the material object. In order to reduce the product expression, (1) is converted into the logarithmic form, as shown:

$$s = l + r \tag{2}$$

where $s = \log(S)$, $l = \log(L)$, and $r = \log(R)$. For a multiband image, the retinex generates the reflectance component, channel by channel [6,18]. Accordingly, all the correction models in this paper are also carried out channel by channel.

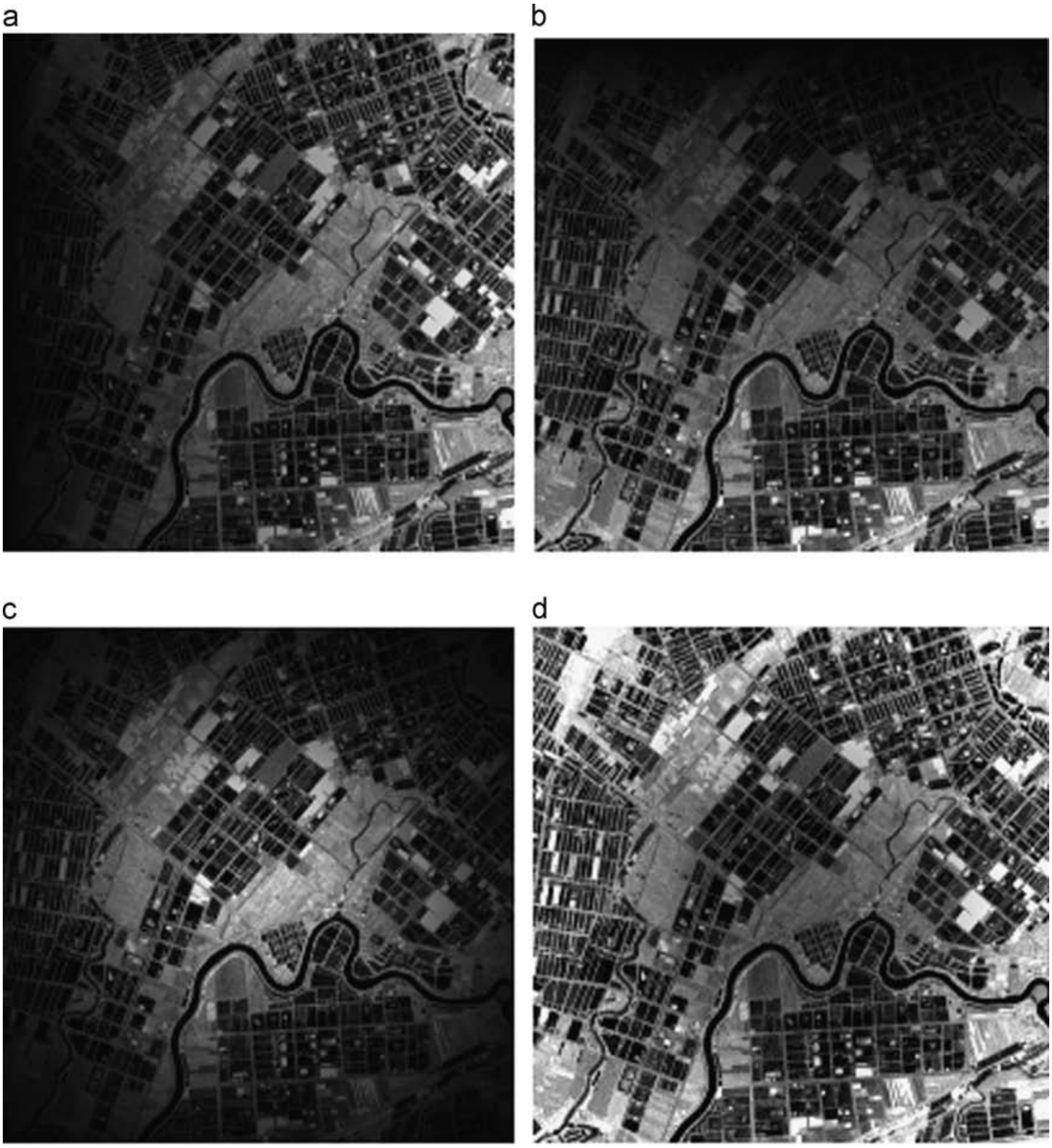

Fig. 3. The four different cases of degradation: (a) horizontal, (b) vertical, (c) Gaussian-1 and (d) Gaussian-2.

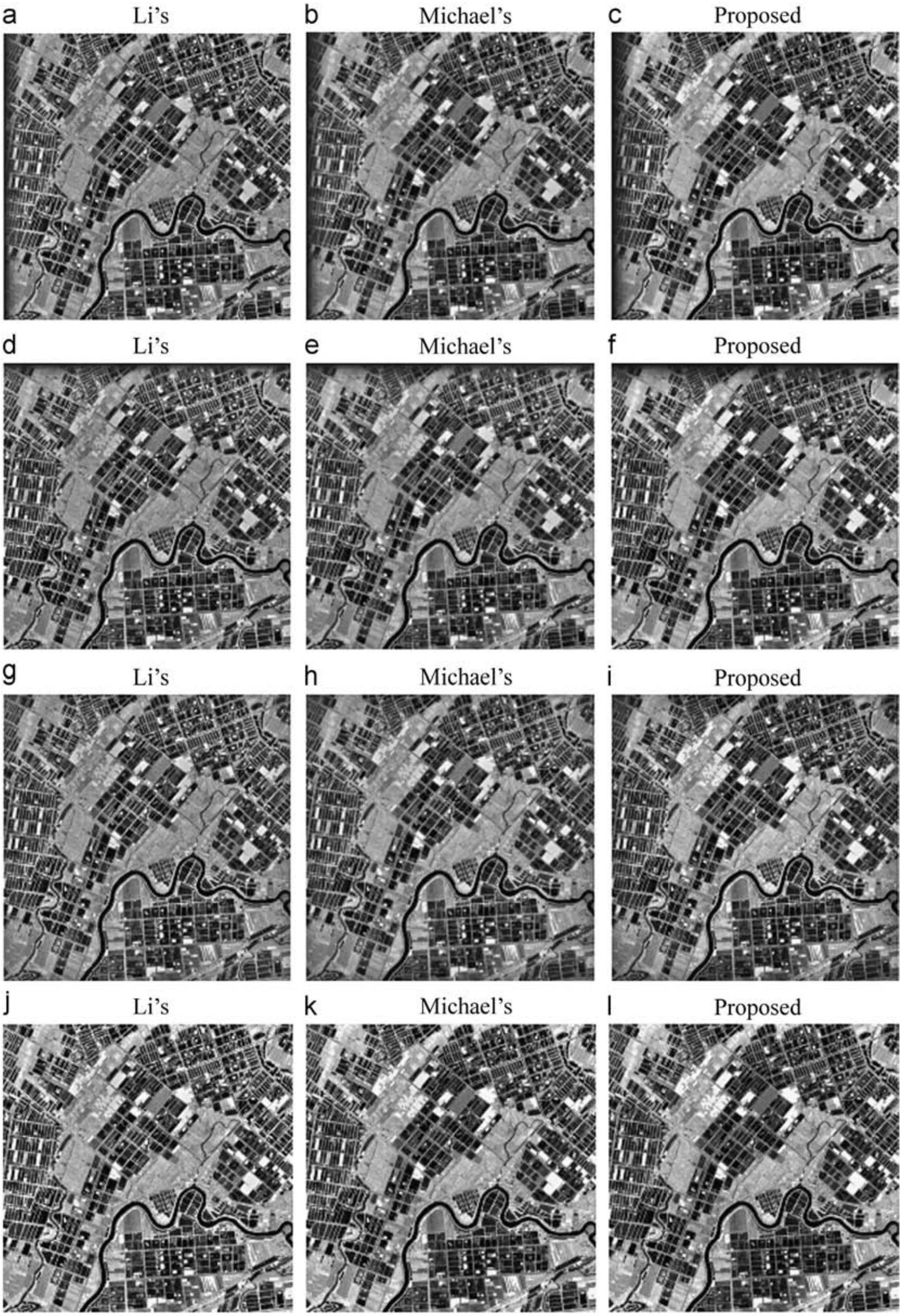

Fig. 4. The corrected results for the four degradation cases. *Top row*: The corrected results for the horizontal degradation. *Second row*: The corrected results for the vertical degradation. *Third row*: The corrected results for the Gaussian-1 degradation. *Bottom row*: The corrected results for the Gaussian-2 degradation.

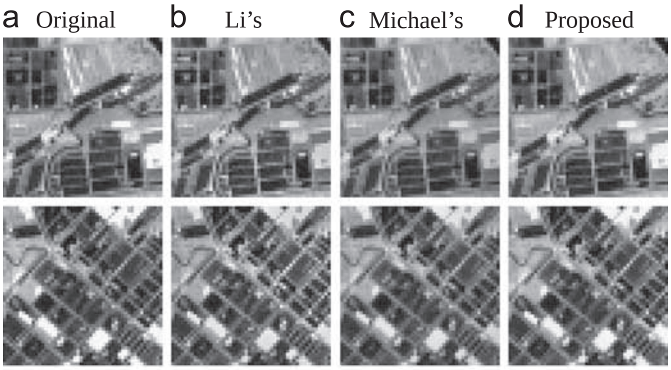

Horizontal

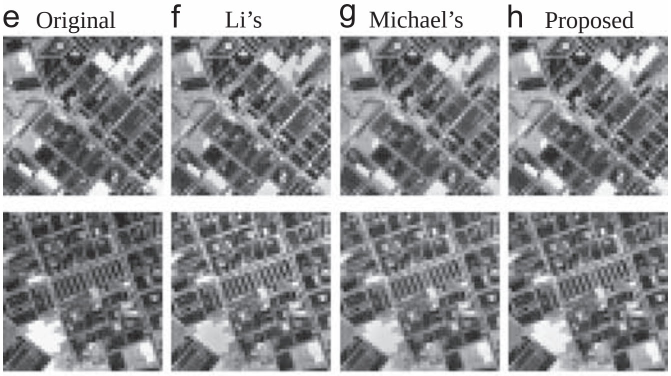

Vertical

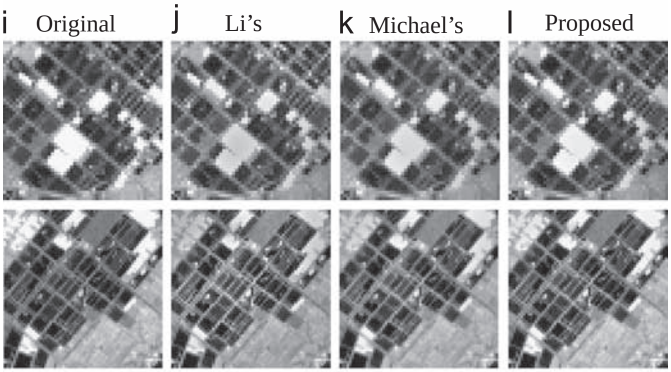

Gaussian-1

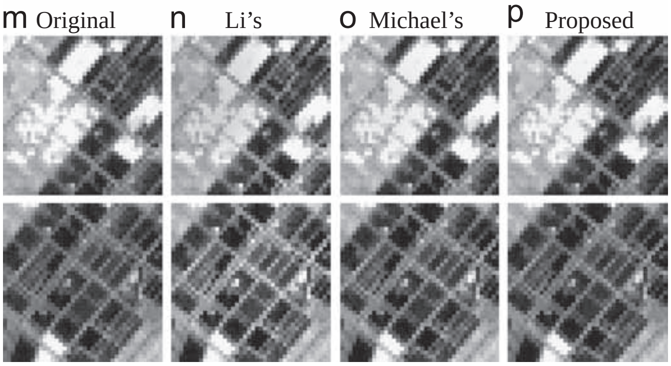

Gaussian-2

Fig. 5. Detailed regions cropped from the original image of Figs. 2(a) and 4. The detailed regions (a), (e), and (i) are cropped from Fig. 2(a). Horizontal: the detailed regions (b)–(d) are cropped from Fig. 4(a)–(c), respectively. Vertical: the detailed regions (f)–(h) are cropped from Fig. 4(d)–(f), respectively. Gaussian-1: the detailed regions (j)–(l) are cropped from Fig. 4(g)–(i), respectively. Gaussian-2: the detailed regions (m)–(p) are cropped from Fig. 4(j)–(l), respectively.

2.2. *The perceptually inspired variational model*

Li et al. [6] proposed a perceptually inspired variational model to directly restore the reflectance and to adjust the uneven intensity distribution in remote sensing images. The perceptually inspired variational model can be shown as follows:

$$\min E(r) = \sum_{\Omega}(||\nabla(r-s)||^2 + \lambda_1||\nabla r||^p + \lambda_2[\exp(r)-1/2]^2)$$
$$p = \begin{cases} 2 & \text{if } x \in \text{Nonedges} \\ 1 & \text{if } x \in \text{Edges} \end{cases}, \ \text{s.t.} r \le 0 \tag{3}$$

where λ_1 and λ_2 are positive parameters to trade off the contribution rates of the second and the last terms in the energy function (3). The constraint $r \le 0$ is derived from the physical characteristics of the reflectance $0 \le R \le 1$.

However, the relationship and the fidelity term between the illumination and reflectance are not considered. This may result in the recovered value deviating significantly from the actual reflectance. Besides, Li et al. [6] divided the spatial domain into edges and non-edges in the regularization term, which belongs to hard segmentation. Thus, we propose a spatially adaptive retinex variational model, which is described in the next section.

3. The spatially adaptive retinex variational model

3.1. *The proposed model*

In [32], Michael et al. assumed that the reflectance component was piecewise constant, and used the TV prior as the regularization term. In this paper, the same assumption is adopted.

In addition, it is very important to note that the TV regularization strength of the reflectance should be associated with the spatial information of the reflectance. In the edge pixels, a weak regularization strength is enforced to preserve detail, and in the homogeneous area, a strong regularization strength is enforced to eliminate the uneven intensity [35–39]. Thus, we construct a spatially adaptive regularization parameter w according to the gradient information. The proposed spatially adaptive retinex variational model can therefore be shown as follows:

$$\min E(r,l) = \sum_{\Omega}[||s-l-r||^2 + \alpha||\nabla l||^2 + \mu w||\nabla r|| + \beta[\exp(r)-0.5]^2]$$
$$\text{s.t.} \quad l \ge s, r \le 0 \tag{4}$$

where α, μ, and β are positive parameters, which control each item in the proposed model, and the term $\sum_{\Omega}||s-l-r||^2$ is used for the fidelity term between the illumination and the reflectance. The constraints are derived from the physical characteristics of the reflectance $0 \le R \le 1$.

The constructed w is a weight parameter, which controls the TV regularization strength of the reflectance, as defined in the following:

$$w(x) = \frac{1}{1+||\nabla r(x)||/k} \tag{5}$$

where k is a nonnegative parameter, which is set to the standard deviation of the reflectance's gradient image, i.e., $k = std(||\nabla r||)$. Therefore, in the cost function (4), there is a unique weight $w(x)$ corresponding to each pixel x. The larger the gradient $||\nabla r(x)||$ is, the smaller the corresponding weight $w(x)$ is, i.e., a weaker regularization strength is enforced to preserve detail. Thus, according to the different gradient information, the regularization strength is spatially adaptive, which is superior to the hard segmentation approach in the work of Li et al. [6].

3.2. *The split Bregman algorithm for the proposed model*

Here, our aim is to minimize the cost function (4). Since two unknown variables exist in (4), an alternating minimization scheme [32,40–43] is used. The minimization problem (4) is converted to two subproblems in the following:

$$\min_r E_1(r) = \sum_{\Omega}[||s-l-r||^2 + \beta[\exp(r)-0.5]^2 + \mu w||\nabla r||] \tag{6}$$

$$\min_l E_2(l) = \sum_{\Omega}[||s-l-r||^2 + \alpha||\nabla l||^2] \tag{7}$$

The basic procedure for the alternating minimization is shown in Fig. 1. The next task is to solve the two subproblems (6) and (7).

The split Bregman algorithm [32,44] is a very efficient way to solve the minimization subproblem in (6). By introducing a new variable, the subproblem (6) is converted into the following constrained problem:

$$\min_{r,d}\left\{\sum_{\Omega}[||s-l^i-r||^2 + \beta[\exp(r)-0.5]^2 + \mu w||d||]\right\} \quad \text{s.t. } d = \nabla r \tag{8}$$

In order to solve the constrained problem, an L2 penalty term is added to get an unconstrained problem:

$$\min_{r,d}\left\{\sum_{\Omega}[||s-l^i-r||^2 + \beta[\exp(r)-0.5]^2 + \mu w||d|| + \lambda||d-\nabla r-b||^2]\right\} \tag{9}$$

where λ is a nonnegative parameter, and b is the Bregman parameter. The other parameters in (9) are the same as in (4). The computation procedure is detailed in Algorithm 1.

Table 1
The quantitative evaluation results for the Wuhan image.

Case	Method	PSNR	MSE	SSIM	GSIM
Horizontal	Li's	21.15	499.38	0.9525	0.9916
	Michael's	22.55	361.24	0.9671	0.9935
	Proposed	**23.36**	**300.31**	**0.9716**	**0.9938**
Vertical	Li's	20.97	519.52	0.9529	0.9916
	Michael's	22.23	389.11	0.9649	0.9936
	Proposed	**22.95**	**329.31**	**0.9722**	**0.9939**
Gaussian-1	Li's	21.23	489.75	0.9484	0.9925
	Michael's	22.88	334.65	0.9651	0.9946
	Proposed	**23.87**	**266.90**	**0.9735**	**0.9953**
Gaussian-2	Li's	22.62	355.63	0.9621	0.9941
	Michael's	24.96	207.47	0.9802	0.9968
	Proposed	**25.97**	**164.39**	**0.9862**	**0.9977**

Algorithm 1.

Step 1: Initialize $u^0=0$, $j=0$, and $b^0=(b_h^0,b_v^0)=0$, where "h" and "v" stand for the horizontal axis and the vertical axis, respectively.

Step 2: Firstly, given u^j and b^j, update d^{j+1} as follows:

$$d^{j+1}=shrinkage\left(\nabla u^j+b^j,\frac{\mu W}{2\lambda}\right) \tag{10}$$

where *shrinkage* is the soft shrinkage operator, defined as

$$shrinkage(z,\theta)=\frac{z}{||z||}\cdot \max\{||z||-\theta,0\} \tag{11}$$

Secondly, update u^{j+1} by minimizing the differentiable optimization problem in the following:

$$\min_u\left\{\sum_\Omega[||s-l^i-u||^2+\beta[\exp(u)-0.5]^2+\lambda||d^{j+1}-\nabla u-b^j||^2]\right\} \tag{12}$$

which can be solved by the Fourier transform, the Gauss–Seidel method, etc. Here, we use the Fourier transform to solve it by

$$u^{j+1}=F^{-1}\left\{\frac{F(s-l^i)-\beta(F(\exp(u^j)\cdot(\exp(u^j)-0.5)))+\lambda G}{1+\lambda(F^*(\nabla_h)F(\nabla_h)+F^*(\nabla_v)F(\nabla_v))}\right\} \tag{13}$$

where F and F^{-1} are the Fourier transformation and the inverse Fourier transformation, respectively. G is denoted as

$$G=F^*(\nabla_h)F(d_h^{j+1}-b_h^j)+F^*(\nabla_v)F(d_v^{j+1}-b_v^j) \tag{14}$$

Thirdly, update as follows:

$$b^{j+1}=b^j-(d^{j+1}-\nabla u^{j+1}) \tag{15}$$

Step 3: If $(||u^{j+1}-u^j||/||u^{j+1}||)\le\varepsilon_u$, $r^{i+1/2}=u^{j+1}$; otherwise, go back to Step 2.

Table 2
The quantitative evaluation results for the Washington DC image.

Case	Method	PSNR	MSE	SSIM	GSIM
Horizontal	Li's	23.36	300.28	0.9613	0.9920
	Michael's	24.41	235.78	0.9645	0.9932
	Proposed	**25.28**	**192.78**	**0.9739**	**0.9952**
Vertical	Li's	24.84	213.17	0.9696	0.9942
	Michael's	25.72	174.41	0.9734	0.9953
	Proposed	**26.31**	**152.24**	**0.9796**	**0.9962**
Gaussian-1	Li's	23.18	312.88	0.9691	0.9960
	Michael's	24.29	242.37	0.9721	0.9963
	Proposed	**25.14**	**199.15**	**0.9760**	**0.9971**
Gaussian-2	Li's	23.76	273.27	0.9560	0.9914
	Michael's	25.26	193.69	0.9671	0.9937
	Proposed	**26.07**	**160.83**	**0.9738**	**0.9954**

Since the subproblem (7) is a differentiable optimization problem, it can also be solved by the Fourier transform, the Gauss–Seidel method, etc. The solution is shown in the following by Fourier transform:

$$l^{i+1/2}=F^{-1}\left(\frac{F(s-r^{i+1})}{1+\alpha(F^*(\nabla_h)F(\nabla_h)+F^*(\nabla_v)F(\nabla_v))}\right) \tag{16}$$

Finally, we give the overall procedure for solving the proposed model in the following:

(1) Given the input image s, initialize $l^0=s$. For $i=0,1,2,\ldots,$
(2) Given l^i, solve the subproblem (6) to get $r^{i+1/2}$ by using Algorithm 1. Then, update r^{i+1} by $r^{i+1}=\min\{r^{i+1/2},0\}$.
Given r^{i+1}, solve the subproblem (7) to get $l^{i+1/2}$ by (16). Then, update l^{i+1} by $l^{i+1}=\max\{l^{i+1/2},s\}$.
(3) Go back to (2) until $(||r^{i+1}-r^i||/||r^{i+1}||)\le\varepsilon_r$ and $\left(||l^{i+1}-l^i||/||l^{i+1}||\right)\le\varepsilon_r$ are satisfied.

By the alternating minimization scheme and the split Bregman algorithm, the minimization problem (4) is solved. Thus, the reflectance component r is recovered in the logarithmic domain. It is then converted to the reflectance R in the spatial domain.

4. Experimental results and discussion

In this section, extensive simulated experiments and real-life experiments are presented to verify the effectiveness of the proposed model. In this paper, we compare the results of the proposed model with the models of

Fig. 6. The corrected results for the horizontal degradation case.

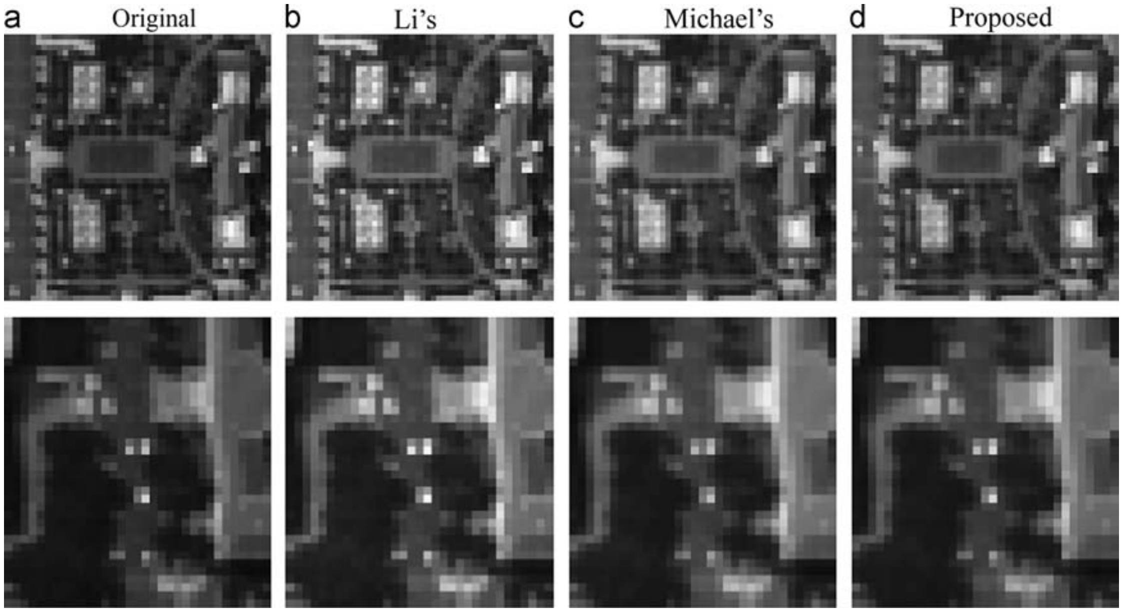

Fig. 7. Detailed regions cropped from the original image of Figs. 2(b) and 6.

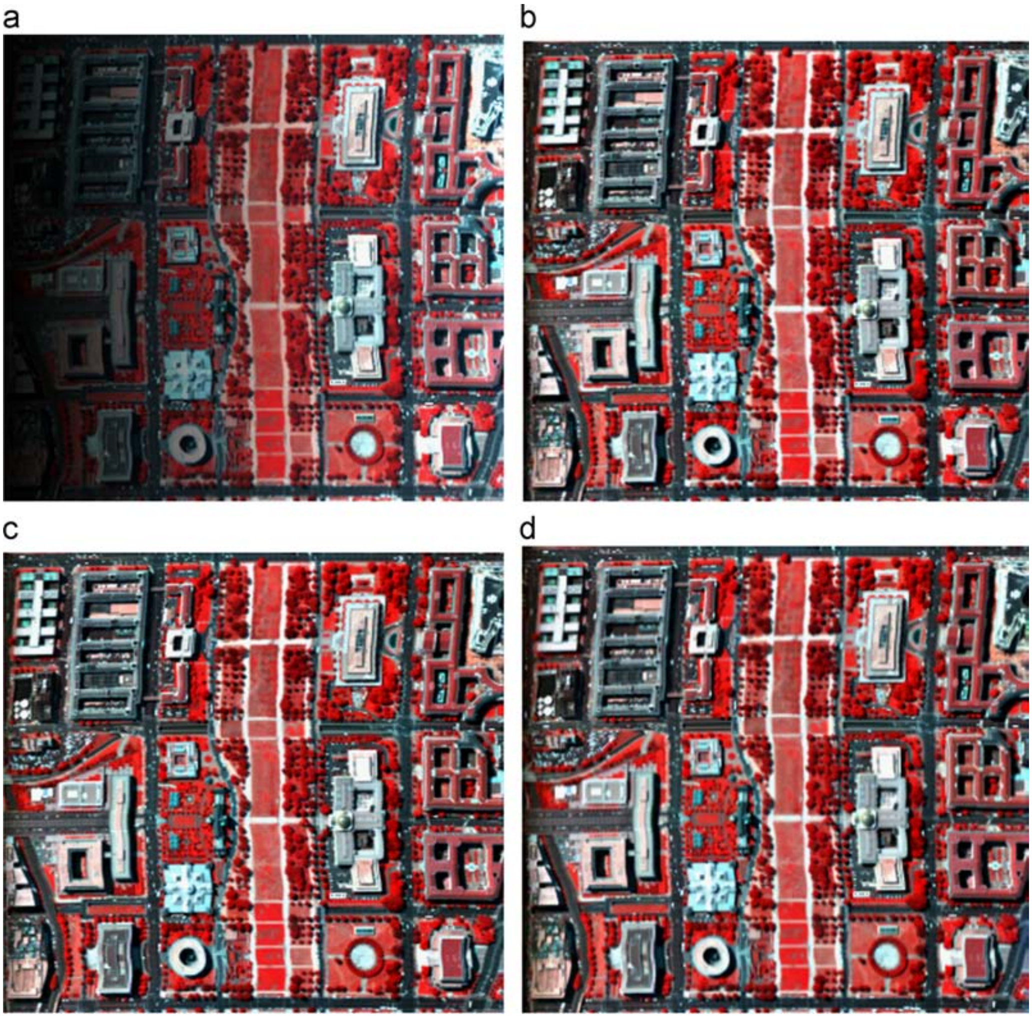

Fig. 8. The results of Spectral fidelity: (a) the degraded image, (b) Li's, MSA=4.1, (c) Michael's, MSA=3.9, and (d) Proposed, MSA=3.5.

Michael's model [32] and Li's model [6]. In the simulated experiments, four common quantity evaluation indexes (PSNR [6,45], MSE [6,46], SSIM [47], GSIM [48]) based on the reference image are used to evaluate the recovery results. Since clear images in real-life experiments are hard to obtain, the above quantity evaluation indexes based on a reference are invalid. Thus, a non-reference image evaluation indicator, the Q-metric [38,49,50], is selected as the objective evaluation for the real-life experiments, which is defined as

$$Q = s_1 \frac{s_1 - s_2}{s_1 + s_2} \tag{17}$$

where s_1 and s_2 are the singular values of the gradient matrix Gr over an $N \times N$ patch (window) w_i. The gradient matrix is defined as

$$Gr = \begin{bmatrix} \vdots & \vdots \\ \nabla_h(q) & \nabla_v(q) \\ \vdots & \vdots \end{bmatrix}, \quad q \in w_i \tag{18}$$

where q denotes the qth pixel in the patch (window) w_i. In all the experiments, the regularization parameter and the other parameters are heuristically adjusted until the best result is obtained.

4.1. Simulated experiments

A Landsat TM image from Wuhan in China was chosen as the standard image. A 200×200 subset from the standard image was selected for the subsequent simulated experiments, as shown in Fig. 2(a). Four different cases of degradation were applied, comprising horizontal, vertical, Gaussian-1 and Gaussian-2 degradation, as shown in Fig. 3 (a)–(d), respectively. The parameters were set as $\alpha = 4, 4, 2, 3$, $\beta = 0.06, 0.06, 0.03, 0.01$, $\mu = 0.04, 0.03, 0.001, 0.001$, and $\lambda = 0.02, 0.019, 0.015, 0.015$ for the four different cases of degradation, respectively.

For the four degradation cases, Fig. 4 shows the corrected results by Michael's model [32], Li's model [6], and the proposed model. It is shown that the corrected result by the proposed method is close to the original image. In order to better display the comparative visual results, detailed regions cropped from the original image Figs. 2(a) and 4 are depicted in Fig. 5. It is found that the proposed method can effectively preserve edges and

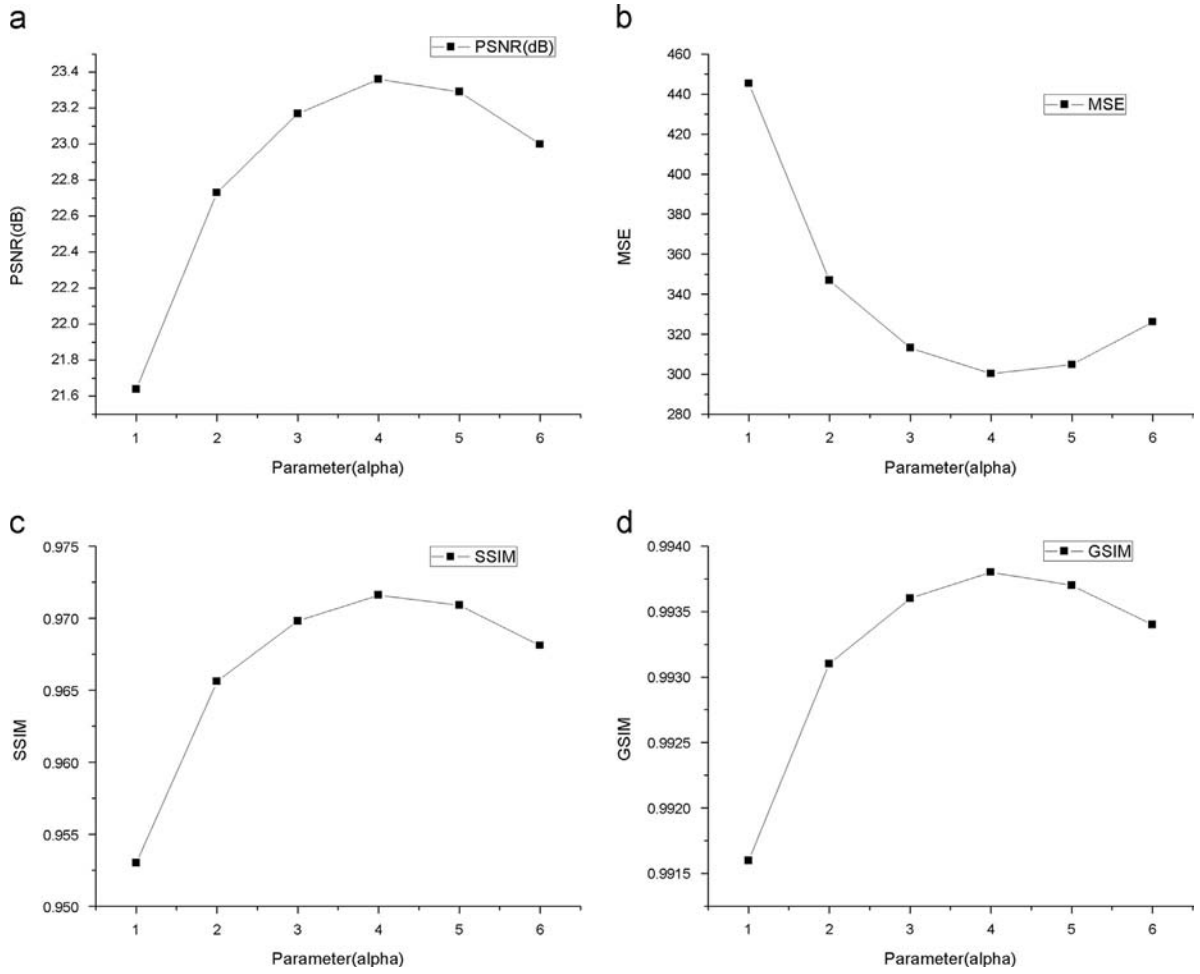

Fig. 9. Quantitative assessment of different values of parameter α for the horizontal degradation of the Wuhan image: (a) PSNR, (b) MSE, (c) SSIM, and (d) GSIM.

correct the intensity so that it is close to the original standard intensity. The reason for this is as follows. Firstly, the spatially adaptive regularization is adopted in the proposed method. The TV regularization strength of the reflectance varies with the spatial information in the process, and thus both details and edges are preserved. Secondly, the GW is used to control the global intensity dispersion. Thirdly, the relationship and the fidelity term between the illumination and reflectance are considered, which ensures that the intensity of the corrected results is close to the original standard intensity. In addition, it can be seen that the visual effect in Fig. 4 is consistent with the quantitative evaluation results in Table 1. That is to say, the proposed method outperforms the other comparative methods, based on both the visual effect and the quantitative assessment.

In order to further test the effectiveness of the proposed method, another simulated data set was applied. The second original image was chosen from a Washington DC data set acquired by the HYDICE sensor. A 307 × 280 subset and one band from the original standard image were selected for the subsequent simulated experiments, as shown in Fig. 1(b). Four different cases of degradation were applied, comprising horizontal, vertical, Gaussian-1 and Guassian-2 degradation. The parameters were set as $\alpha = 4, 4, 3, 4$, $\beta = 0.02, 0.02, 0.03, 0.02$, $\mu = 0.2, 0.2, 0.09, 0.07$, and $\lambda = 0.022, 0.019, 0.03, 0.03$ for the four different cases of degradation, respectively.

A quantitative comparison of the results using the four common quantity evaluation indexes is shown in Table 2. From the comparison of the results, it can be clearly seen that the proposed method performs better than the other methods. Moreover, a visual comparison of the results is also given. To save space, only the horizontal case of degradation is displayed in Fig. 6. To clearly display the comparative visual results, detailed regions cropped from the original image of Figs. 2(b) and 6 are depicted in Fig. 7.

Table 3
The quantitative evaluation results for the three real-life experiments.

Image	Li's	Michael's	Proposed
Data 1	63.92	66.93	**68.25**
Data 2	60.11	61.12	**62.98**
Data 3	14.65	16.34	**17.72**

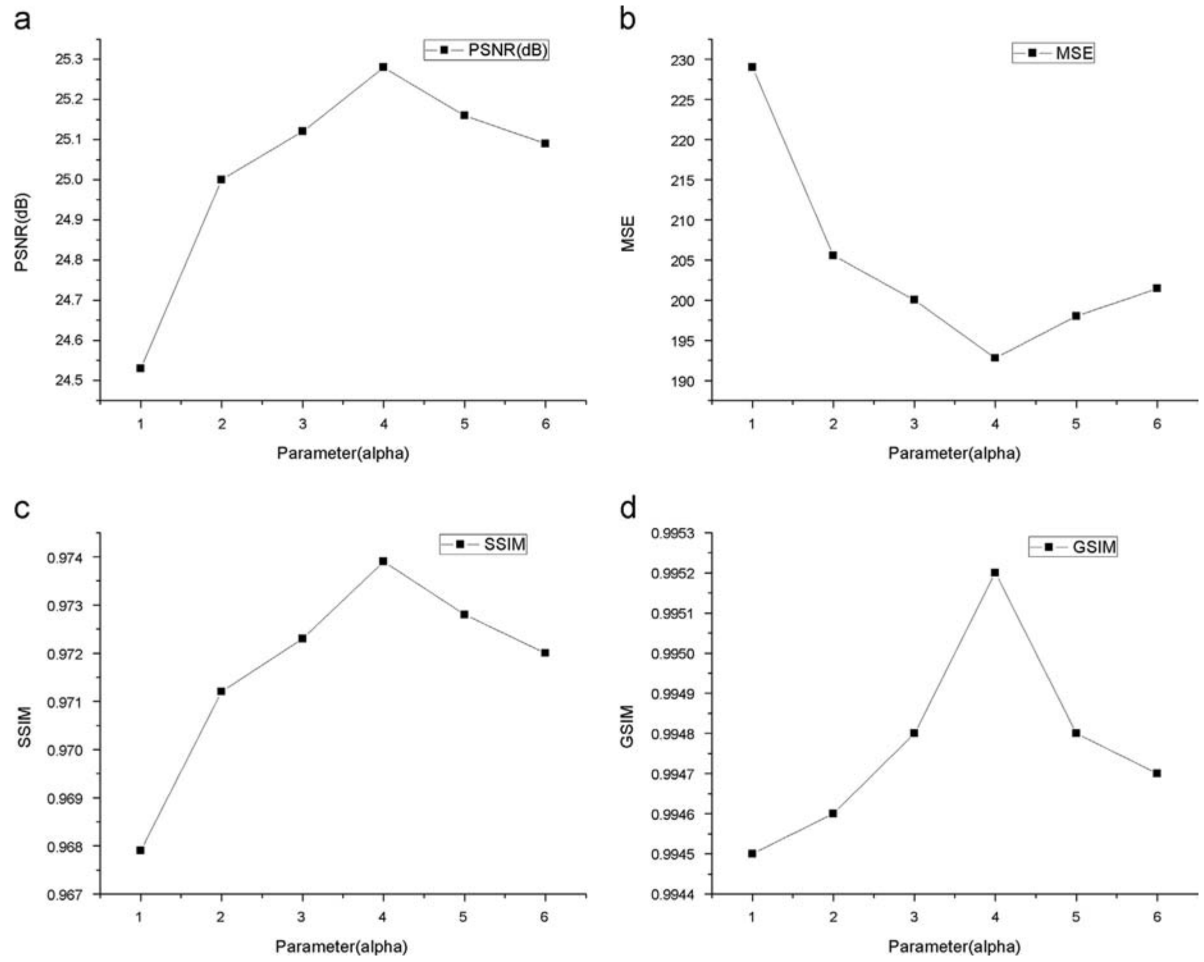

Fig. 10. Quantitative assessment of different values of parameter α for the horizontal degradation of the Washington DC image: (a) PSNR, (b) MSE, (c) SSIM, and (d) GSIM.

It can again be seen that the proposed method outperforms the other methods, which is consistent with the quantitative evaluation results in Table 2. In summary, the proposed method can efficiently adjust the uneven intensity distribution, preserve the details, and restore the valid information in remote sensing images.

To test the spectral fidelity of the proposed method, it was applied to process multiband images. The three selected bands are shown in Fig. 8. The horizontal case of degradation is shown in Fig. 8(a). To evaluate the spectral quality of the corrected images, the spectral angle (SA) is selected, which is defined as

$$\theta(x) = \cos^{-1}\left[\frac{\overrightarrow{X}.*\overrightarrow{Y}}{||\overrightarrow{X}||*||\overrightarrow{Y}||}\right] \tag{19}$$

where $\overrightarrow{X}$ and $\overrightarrow{Y}$ are the spectral vector in each pixel x in the original image and the corrected image, respectively. The mean of the spectral angle (MSA) is used to evaluate the corrected results. A lower MSA value can reflect a better spectral fidelity. From the results in Fig. 8, it can be seen that the proposed method has the lowest MSA

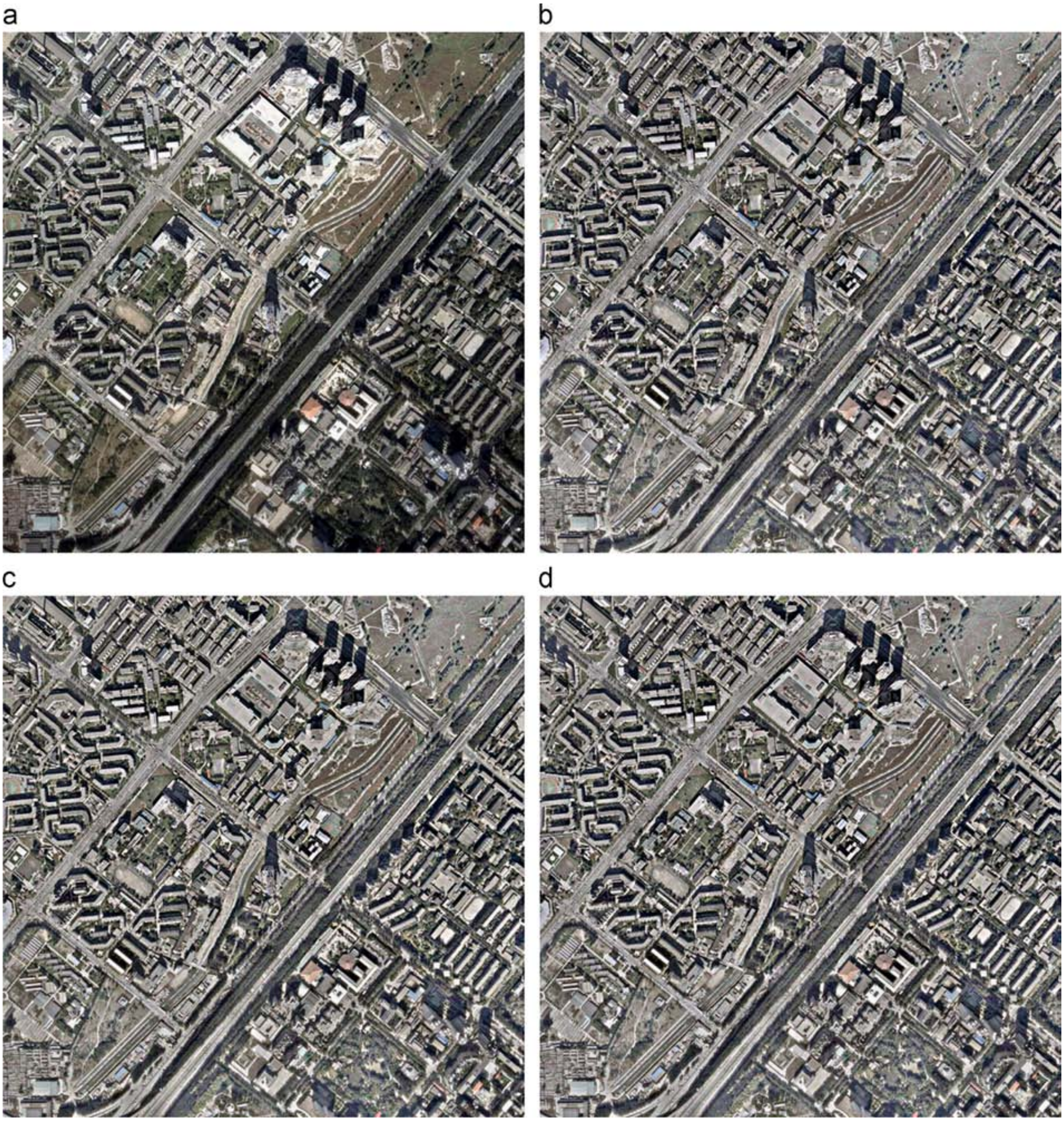

Fig. 11. Results for the first real image: (a) original aerial image, (b) Li's method, (c) Michael's method and (d) the proposed method.

value, which demonstrates that the proposed method is better at preserving the spectral fidelity than the other methods.

Finally, we intend to discuss how the performance is influenced by the parameters. Through a series of different experiments, each parameter is varied within a certain range. Here, we give an example to study the performance with different values of parameter α. In Fig. 9, the performance curve is shown with different values of parameter α for the Wuhan image. In Fig. 10, the performance curve

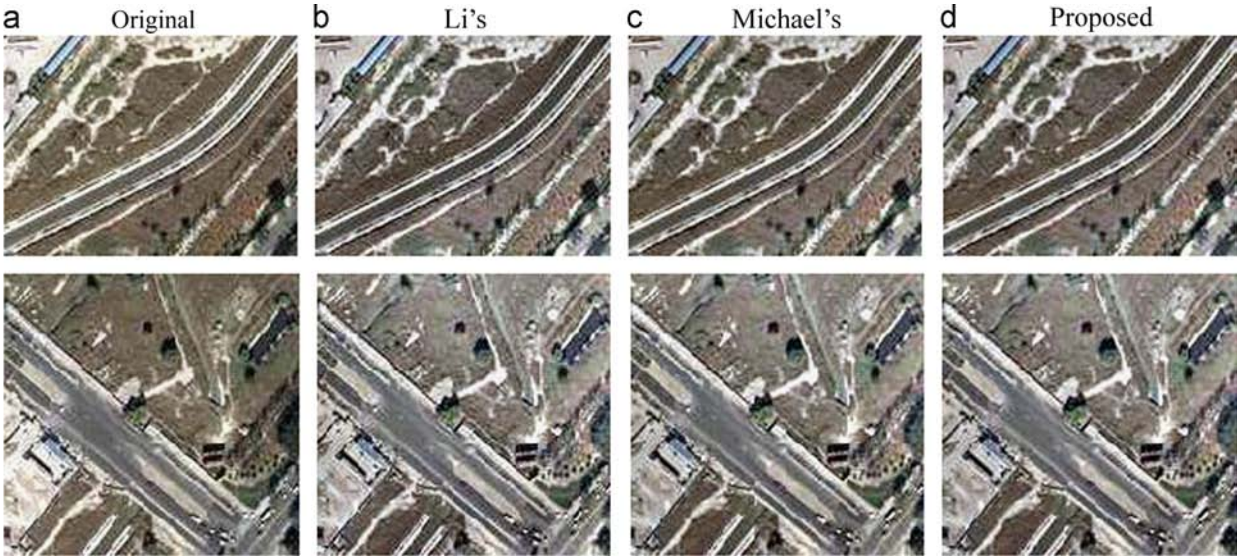

Fig. 12. Detailed regions (a)–(d) cropped from Fig. 11(a)–(d).

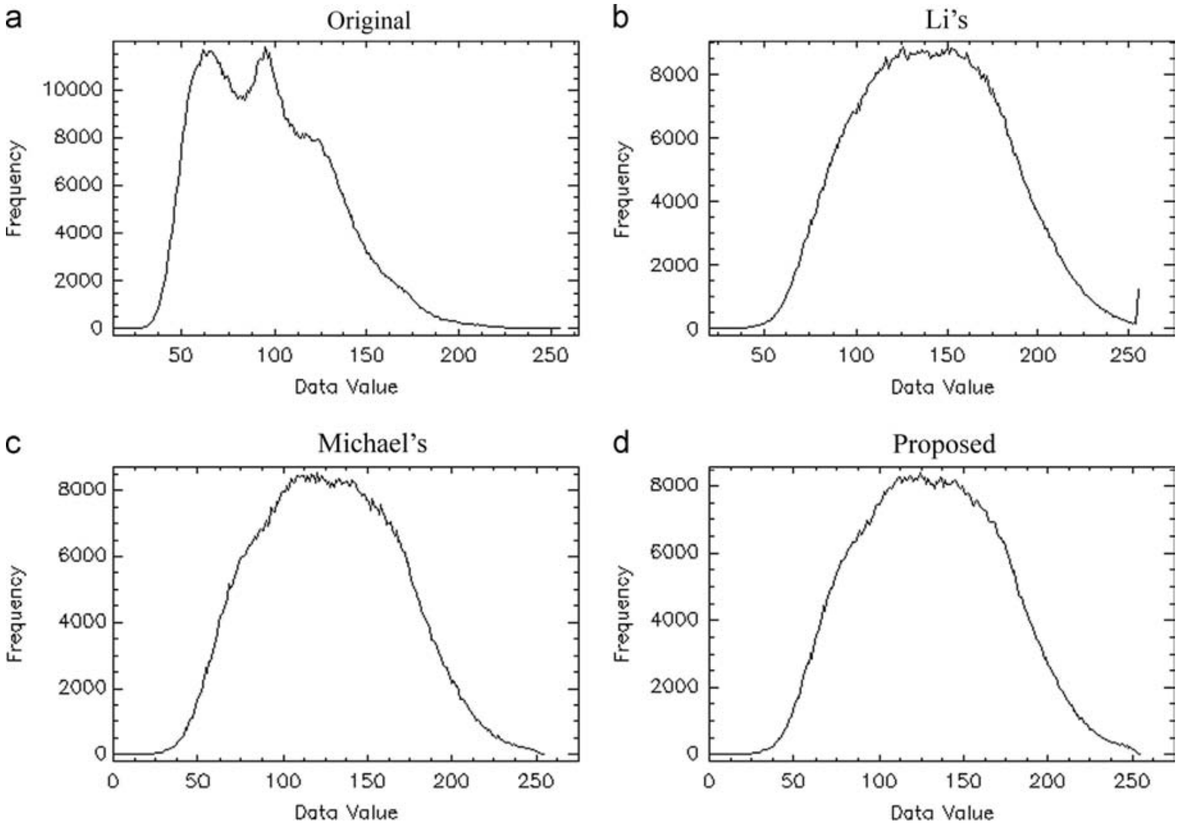

Fig. 13. Histograms of Fig. 11(a)–(d).

is shown with different values of parameter α for the Washington DC image. In both cases, it can be seen that the optimal performance is acquired at a certain point on the curve.

4.2. Real-life experiments

In order to verify the performance of the proposed method with real data, the proposed method was tested on three real aerial remote sensing images. A quantitative comparison of the results using a non-reference image evaluation indicator, the Q-metric, is shown in Table 3. Here, it is again found that the proposed method outperforms the other methods. The comparison details are shown in the following.

The first real image, with a size of 1000×1000, is shown in Fig. 11(a). Due to the uneven distribution of the ambient lighting, the luminance of the buildings in the lower-right corner is darker than that of the buildings in the top-left corner. This results in color distortion and the details being lost.

For the first real image, the parameters were set as $\alpha = 2$, $\beta = 0.02$, $\mu = 0.1$, and $\lambda = 0.01$. Fig. 11(b)–(d) show the corrected results by Li's model [32], Michael's model [6], and the proposed model, respectively. The results demonstrate that the three methods can all adjust the uneven intensity distribution in the original image, but some regions in Fig. 11(b) are more exposed than the ones in Fig. 11(c) and (d). In order to illustrate this point, detailed regions cropped from Fig. 11 are shown in Fig. 12. The result in Fig. 12(b) is brighter than the result in Fig. 12(c) and (d). Objectively, from the histograms shown in Fig. 13, it can be seen that Fig. 13(b)–(d) are flatter than Fig. 13(a), but a leap exists in the tail of Fig. 13(b), which results in the overexposed phenomenon in Fig. 11(b), whereas both Fig. 13(c) and (d) have a high similarity to the Gaussian distribution. However, the curve in Fig. 13(d) is much smoother and much more similar to the Gaussian distribution than Fig. 13(c). This is attributed to the spatially adaptive regularization in the proposed model, which is used to constrain the TV regularization strength of the reflectance, according to the spatial information. In addition, we can see that the proposed method produces the highest Q-metric values, as shown in Table 3, which is consistent with the visual results.

The second real image, with a size of 950×600, is shown in Fig. 14(a). The parameters were set as $\alpha = 3$, $\beta = 0.03$, $\mu = 0.4$, and $\lambda = 0.01$. The corrected results of the Li's method, Michael's method, and the proposed method are shown in Fig. 14(b)–(d), respectively. Detailed regions cropped from Fig. 14 are shown in Fig. 15.

The third real image, with a size of 600×400, is shown in Fig. 16(a). The parameters were set as $\alpha = 2$, $\beta = 0.04$, $\mu = 0.3$, and $\lambda = 0.025$. The corrected results and their detailed regions are shown in Figs. 16 and 17, respectively. The quantitative evaluation results using the Q-metric

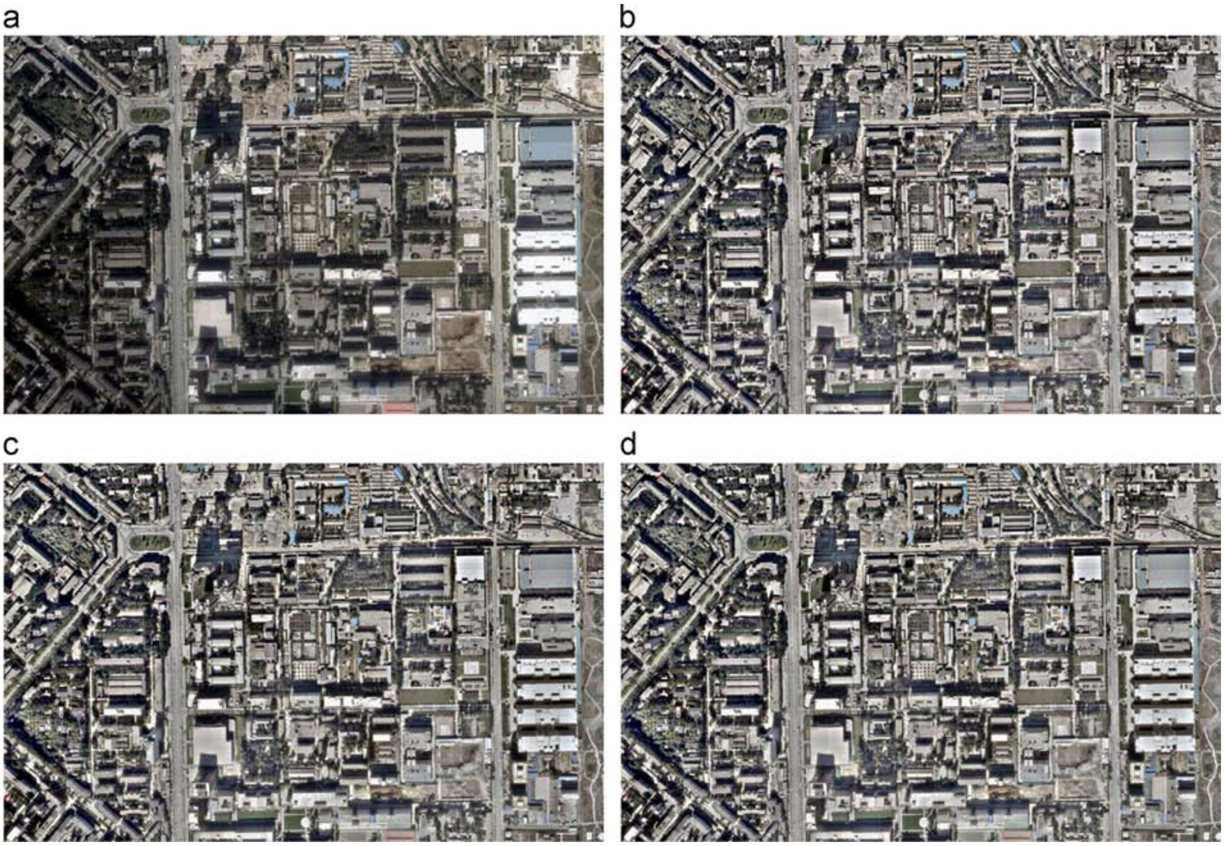

Fig. 14. Results for the second real image. (a) Original aerial image. (b) Li's method. (c) Michael's method. (d) the proposed method.

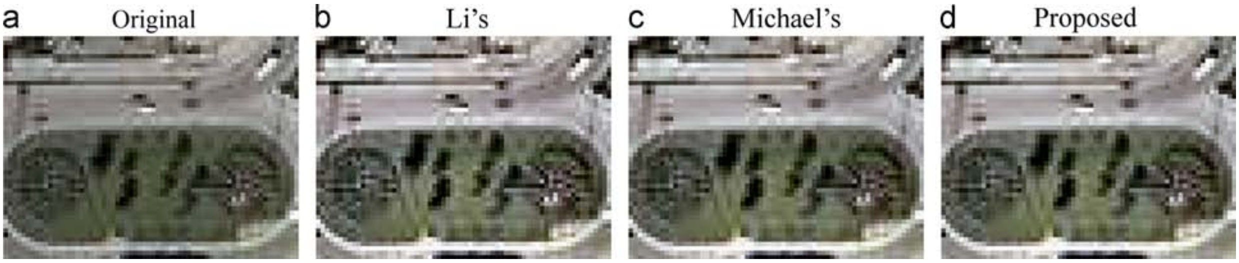

Fig. 15. Detailed regions (a)–(d) cropped from Fig. 14(a)–(d).

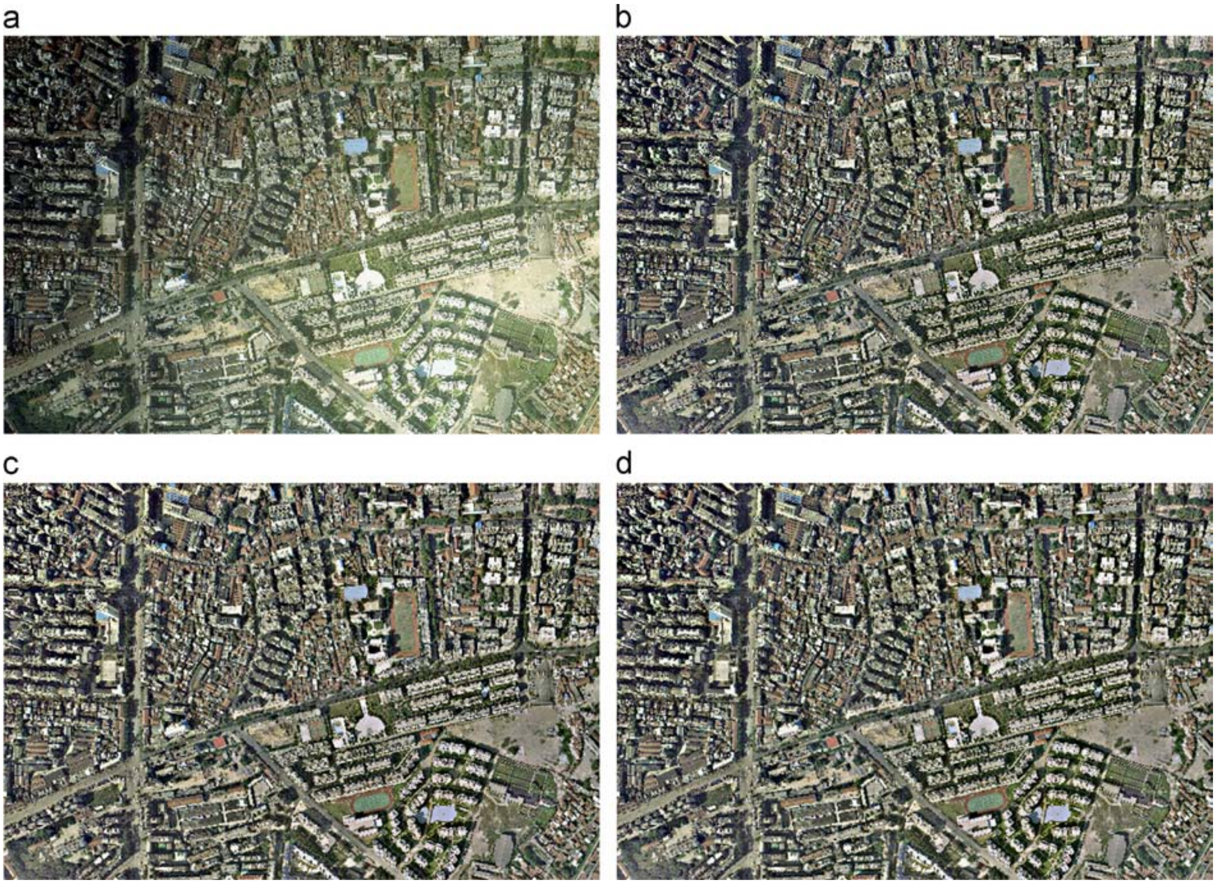

Fig. 16. Results for the third real image: (a) original aerial image, (b) Li's method, (c) Michael's method and (d) The proposed method.

Fig. 17. Detailed regions (a)–(d) cropped from Fig. 16(a)–(d).

index for these three real-life experiments are shown in Table 3. It can again be seen that the proposed method outperforms the other methods and produces the highest Q-metric values. From the detailed regions in Figs. 15 and 17, it can also be seen that the proposed method preserves the color more effectively.

5. Conclusion

This paper presents a spatially adaptive retinex variational model for uneven intensity correction. In this model, the spatial information is used to constrain the TV regularization strength of the reflectance, which effectively preserves the details. The relationship and the fidelity term between the illumination and reflectance are also considered. Moreover, the split Bregman optimization algorithm is employed to solve the proposed model. Extensive experiments were undertaken with both simulated data and real-life data. In summary, the proposed method can efficiently adjust the uneven intensity distribution in remote sensing images, based on both the visual effect and quantitative assessment. In this paper, we are concerned with the adjustment of the uneven intensity distribution in aerial remote sensing images. For the spectral degradation issue, especially in hyperspectral images, we will study the spectral information in our future work.

Acknowledgements

The authors would like to thank the editors and the anonymous reviewers for their valuable suggestions. This work was supported in part by the Nation Basic Research Program of China (973 Program) under grant no. 2011CB707103, the National Natural Science Foundation of China under Grants 41271376, Hubei Natural Science Foundation under Grant 2011CDA096, Program for Changjiang Scholars and Innovative Research Team in University (IRT1278), and the Fundamental Research Funds for the Central University.

References

[1] R.S. Fraser, O.P. Bahethi, A. Al-Abbas, The effect of the atmosphere on the classification of satellite observations to identify surface features, Remote Sens. Environ. 6 (3) (1977) 229–249.
[2] C. Song, C.E. Woodcock, K.C. Seto, M.P. Lenney, S.A. Macomber, Classification and change detection using Landsat TM data: when and how to correct atmospheric effects? Remote Sens. Environ. 75 (2) (2001) 230–244.
[3] S. Thiemann, H. Kaufmann, Lake water quality monitoring using hyperspectral airborne data—a semiempirical multisensor and multitemporal approach for the Mecklenburg Lake District, Germany, Remote Sens. Environ. 81 (2) (2002) 228–237.
[4] A.P. Craknell, L.W. Hayes, Atmospheric corrections to passive satellite remote sensing data, in: Introduction to Remote Sensing, Taylor & Francis, London, 1993 (Chapter 8).
[5] S.R. Pudale, U.V. Bhosle, Comparative study of relative radiometric normalization techniques for resourcesat1 LISS III sensor images, in: International Conference on Computational Intelligence and Multimedia Applications, 2007, pp. 233–239.
[6] H. Li, L. Zhang, H. Shen, A perceptually inspired variational method for the uneven intensity correction of remote sensing images, IEEE Trans. Geosci. Remote Sens. 50 (8) (2012) 3053–3065.
[7] M. Firdaus Zakaria, H. Ibrahim, S. Azmin Suandi, A review: Image compensation techniques, in: Proceedings of the 2nd International Conference on Computer Engineering and Technology (ICCET), 2010, pp. V7-404–V7-408.
[8] M. Dileep, A.S. Murthy, A comparison between different colour image contrast enhancement algorithms, in: Proceedings of the International Conference on Emerging Trends in Electrical and Computer Technology (ICETECT), 2011, pp. 708–712.
[9] A.K. Vishwakarma, A. Mishra, Color image enhancement techniques: a critical review, Indian J. Comput. Sci. Eng. 3 (2012) 39–45.
[10] N. Sengee, H. Choi, Brightness preserving weight clustering histogram equalization, IEEE Trans. Consum. Electron. 54 (3) (2008) 1329–1337.
[11] H. Yeganeh, A. Ziaei, A. Rezaie, A novel approach for contrast enhancement based on histogram equalization, in: International Conference on Computer and Communication Engineering (ICCCE), 2008, pp. 256–260.
[12] G. Thomas, D. Flores-Tapia, S. Pistorius, Histogram specification: a fast and flexible method to process digital images, IEEE Trans. Instrum. Meas. 60 (5) (2011) 1565–1578.
[13] N. Sengee, A. Sengee, H.K. Choi, Image contrast enhancement using bi-histogram equalization with neighborhood metrics, IEEE Trans. Consum. Electron. 56 (4) (2010) 2727–2734.
[14] S. Sarkar, G. Healey, Hyperspectral texture synthesis using histogram and power spectral density matching, IEEE Trans. Geosci. Remote Sens. 48 (5) (2010) 2261–2270.
[15] W.K. Pratt, Digital Image Processing, 4th ed. Wiley-Interscience, New York, 2007.
[16] M. Song, D. Tao, C. Chen, J. Bu, J. Luo, C. Zhang, Probabilistic exposure fusion, IEEE Trans. Image Process. 21 (1) (2012) 341–357.
[17] M. Song, D. Tao, C. Chen, X. Li, C.W. Chen, Color to gray: visual cue preservation, IEEE Trans. Pattern Anal. Mach. Intell. 32 (9) (2010) 1537–1552.
[18] E.H. Land, J.J. McCann, Lightness and retinex theory, J. Opt. Soc. Am. 61 (1) (1971) 1–11.
[19] Y.K. Park, S.L. Park, J.K. Kim, Retinex method based on adaptive smoothing for illumination invariant face recognition, Signal Process. 88 (8) (2008) 1929–1945.
[20] D. Marini, A. Rizzi, A computational approach to color adaptation effects, Image Vis. Comput. 18 (13) (2000) 1005–1014.
[21] E. Provenzi, L. De Carli, A. Rizzi, D. Marini, Mathematical definition and analysis of the Retinex algorithm, JOSA A 22 (12) (2005) 2613–2621.
[22] T.J. Cooper, F.A. Baqai, Analysis and extensions of the Frankle–McCann Retinex algorithm, J. Electron. Imaging 13 (1) (2004) 85–92.
[23] T. Chan, J. Shen, Image Processing and Analysis: Variational, PDE, Wavelet, and Stochastic Methods, Society for Industrial and Applied Mathematics, 2005.
[24] M.K. Ng, H. Shen, E.Y. Lam, L. Zhang, A total variation regularization based super-resolution reconstruction algorithm for digital video, EURASIP J. Adv. Signal Process. ; http://dx.doi.org/10.1155/2007/74585.
[25] Q. Yuan, L. Zhang, H. Shen, P. Li, Adaptive multiple-frame image super-resolution based on U-curve, IEEE Trans. Image Process. 19 (12) (2010) 3157–3170.
[26] K. Zhang, X. Gao, D. Tao, X. Li, Single image super-resolution with non-local means and steering kernel regression, IEEE Trans. Image Process. 21 (11) (2012) 4544–4556.
[27] B.K. Horn, Determining lightness from an image, Comput. Graph. Image Process. 3 (4) (1974) 277–299.
[28] A. Blake, Boundary conditions for lightness computation in Mondrian world, Comput. Vis. Graph. Image Process. 32 (3) (1985) 314–327.
[29] D. Terzopoulos, Image analysis using multigrid relaxation methods, IEEE Trans. Pattern Anal. Mach. Intell. 2 (1986) 129–139.
[30] J.M. Morel, A.B. Petro, C. Sbert, A PDE formalization of retinex theory, IEEE Trans. Image Process. 19 (11) (2010) 2825–2837.
[31] R. Kimmel, M. Elad, D. Shaked, R. Keshet, I. Sobel, A variational framework for retinex, Int. J. Comput. Vis. 52 (1) (2003) 7–23.
[32] M.K. Ng, W. Wang, A total variation model for Retinex, SIAM J. Imaging Sci. 4 (1) (2011) 345–365.
[33] E. Provenzi, C. Gatta, M. Fierro, A. Rizzi, A spatially variant white-patch and gray-world method for color image enhancement driven by local contrast, IEEE Trans. Pattern Anal. Mach. Intell. 30 (10) (2008) 1757–1770.
[34] R. Palma-Amestoy, E. Provenzi, M. Bertalmío, V. Caselles, A perceptually inspired variational framework for color enhancement, IEEE Trans. Pattern Anal. Mach. Intell. 31 (3) (2009) 458–474.

[35] D.M. Strong, P. Blomgren, T.F. Chan, Spatially adaptive local-feature-driven total variation minimizing image restoration, in: Proceedings of the Optical Science, Engineering and Instrumentation'97, 1997, pp. 222–233.

[36] Q. Chen, P. Montesinos, Q.S. Sun, P.A. Heng, D.S. Xia, Adaptive total variation denoising based on difference curvature, Image Vis. Comput. 28 (3) (2010) 298–306.

[37] A. Chopra, H. Lian, Total variation, adaptive total variation and nonconvex smoothly clipped absolute deviation penalty for denoising blocky images, Pattern Recognit. 43 (8) (2010) 2609–2619.

[38] Q. Yuan, L. Zhang, H. Shen, Multiframe super-resolution employing a spatially weighted total variation model, IEEE Trans. Circuits Syst. Video Technol. 22 (3) (2012) 379–392.

[39] X. Li, Y. Hu, X. Gao, D. Tao, B. Ning, A multi-frame image super-resolution method, Signal Process. 90 (2) (2010) 405–414.

[40] D. Tao, X. Li, X. Wu, S.J. Maybank, General tensor discriminant analysis and gabor features for gait recognition, IEEE Trans. Pattern Anal. Mach. Intell. 29 (10) (2007) 1700–1715.

[41] T. Zhou, D. Tao, Double shrinking sparse dimension reduction, IEEE Trans. Image Process. 22 (1) (2013) 244–257.

[42] W. Liu, D. Tao, Multiview Hessian regularization for image annotation, IEEE Trans. Image Process. 22 (7) (2013) 2676–2687.

[43] J. Li, D. Tao, Simple exponential family PCA, IEEE Trans. Neural Networks Learn. Syst. 24 (3) (2013) 485–497.

[44] T. Goldstein, S. Osher, The split Bregman method for L1-regularized problems, SIAM J. Imaging Sci. 2 (2) (2009) 323–343.

[45] H. Zhang, L. Zhang, H. Shen, A super-resolution reconstruction algorithm for hyperspectral images, Signal Process. 92 (9) (2012) 2082–2096.

[46] L. Zhang, H. Zhang, H. Shen, P. Li, A super-resolution reconstruction algorithm for surveillance images, Signal Process. 90 (3) (2010) 848–859.

[47] Z. Wang, A.C. Bovik, H.R. Sheikh, E.P. Simoncelli, Image quality assessment: from error visibility to structural similarity, IEEE Trans. Image Process. 13 (4) (2004) 600–612.

[48] A. Liu, W. Lin, M. Narwaria, Image quality assessment based on gradient similarity, IEEE Trans. Image Process. 21 (4) (2012) 1500–1512.

[49] X. Zhu, P. Milanfar, Automatic parameter selection for denoising algorithms using a no-reference measure of image content, IEEE Trans. Image Process. 19 (12) (2010) 3116–3132.

[50] X. Lan, L. Zhang, H. Shen, Q. Yuan, H. Li, Single image haze removal considering sensor blur and noise, EURASIP J. Adv. Signal Process. (1) http://dx.doi.org/10.1186/1687–6180-2013–86.